Shaping MOF Oxime Oxidation Catalyst Through Structure Directing Growth Inside of Chitosan Aerogel Microspheres

Nisrine Hammi,[a,b,c] Shuo Chen,[c] Ana Primo,[b] Sebastien Royer,[c] Hermenegildo Garcia,[b,*] Abdelkrim El Kadib,[a,*]

Metal-organic frameworks stand as unique building-blocks, bridging the gap between coordination chemistry and materials science. While significant advance has been made in their design, current efforts focus on expanding their pore size above the microporous regime and on their shaping into well suitable end use devices. For such a purpose, we herein explored the use of chitosan hydrogel microspheres as a mold to grow an extended network of MOFs, followed by CO_2-supercritical drying to generate three-dimensional polysaccharide nanofibrils embedding entangled MOF nanoclusters. This strategy was found to be highly versatile, allowing the preparation of **HKUST-1@CS**, **ZIF-8@CS**, **ZIF-67@CS** and **Fe-BTC@CS** porous microspheres. The resulting lightweight aerogels display excellent activity for oxime oxidation, with **HKUST-1@CS** standing as the most promising. The vertues of supercritical drying were substantiated by comparing the catalytic activity of these aerogels with their xerogel analogues as well as pristine HKUST-1. Interestingly moreover, the configuration of MOF in chitosan beads precludes the metal from leaching and allows easy recovery of the catalyst from the medium and its possible recycling.

Introduction

Constructed from the expansion of metal ions/inorganic clusters bridged through organic linkers, the so-called metal-organic frameworks (MOFs) have emerged as a molecularly-programmable toolbox in chemistry and materials science.[1] Their high surface area, the presence of reactive metals, defective ligands, and the possible framework functionalization have triggered an extensive use in heterogeneous catalysis, including oxidation and hydrogenation.[2–5] Unfortunately, although a plenty of MOFs with different tunable nanostructures can be obtained using various metal ions and organic linkers,[6] most of them display microporous network that severely limits the transportation and diffusion of substrates from reaching active sites.[7] Native MOF micro-particles are also difficult to recover and reuse in heterogeneous catalysis, making them unsuitable in batch and impracticable in flow.[8] To circumvent these drawbacks, a nascent field raised where MOF particulates are hybridized with other substructures including synthetic polymers and natural biopolymers,[9,10] ceramics,[11] carbon particles,[12] among others.[13] This holistic association brings a set of advantages by : i) expanding the pore size above 2 nm,[14] ii) improving thermal and/or chemical stability,[15] ii) processing the material body into films, monoliths, pallets, ect.,[16] and iv) imparting additional reactivity to the resulting materials.[17] Conceptually speaking, this route is expected to further promote the use of MOFs in industrial technologies, with a special emphasis to applications requiring multifunctional and hierarchical porous frameworks, namely adsorption and heterogeneous catalysis.[18]

Building on these reports and inspired by our own endeavors, we envisioned the growth of MOF substructures using chitosan polysaccharide microspheres. We have previously shown that chitosan could be shaped as porous hydrogels containing a tiny amount of the polysaccharide (~ 2 to 3 wt%) dispersed in nearly 97-98 wt% of the liquid (water for hydrogels and ethanol for alcogels).[19,20] These beads act as a nanoreactor to grow and confine a variety of nano-objects including sol-gel clusters,[21] metal nanoparticles,[22] lamellar montmorillonite clays[23] and exfoliated graphene oxide sheets.[24] CO_2 supercritical drying of the resulting soft hydrogels constitute the driving force to draw them to the realm of dried matter by suppressing the interfacial forces commonly encountered during the challenging step of solvent removal. Supercritical drying consists in eliminating the fluidic CO_2 in its supercritical state, which consequently prevent the wall collapsing and allows for retaining the porous network created in the starting hydrogels.[25,26] This approach presents a considerable interest as most of porous materials (e.g. mesostructured silicates) are prepared using costly-synthesized surfactant as a template, followed by its unsustainable, energetically-demanding destruction to leave the precious open space required for catalysis.[27,28] Surprisingly, while MOF configuration has been the subject of extensive studies, very few studies have hitherto focused on their growth as light-weight porous aerogels,[29] and to the best of our knowledge, none of them have explored the preparation of polysaccharide-MOF aerogels.[27,30]

[a.] *Euromed Research Center, Engineering Division, Euro-Med University of Fes (UEMF), Route de Meknes, Rond-point de Bensouda, 30070, Fès, Morocco. Corresponding author: a.elkadib@ueuromed.org*
[b.] *Instituto de Tecnología Química (CSIC-UPV) and Departamento de Química (UPV), Universitat Politècnica de València, Av. de los Naranjos s/n, 46022 Valencia, Spain*
[c.] *Univ. Lille, CNRS, Centrale Lille, ENSCL, Univ. Artois, UMR 8181 - UCCS - Unité de Catalyse et Chimie du Solide, F-59000 Lille, France.*
Electronic Supplementary Information (ESI) available: [details of any supplementary information available should be included here]. See DOI: 10.1039/x0xx00000x

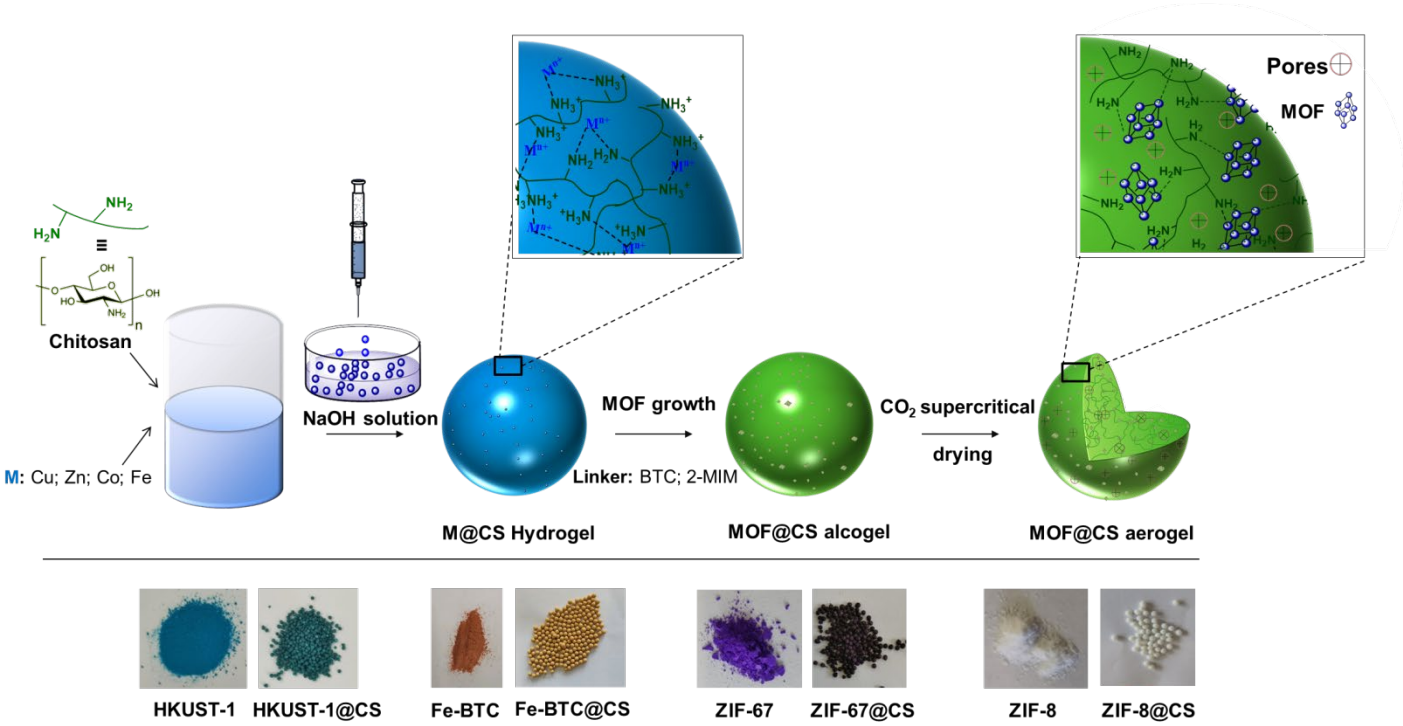

Scheme 1. Illustration of the multistep preparation procedure for **MOF@CS** aerogels. The interplay between the biopolymer, the metal precursor and the ligand is presented along these steps. The digital photos show the native MOF powders and the corresponding **MOF@CS** beads. The color of the hybrid microspheres is due to the MOF grown inside.

Herein, we introduce a strategy for templating the growth of microporous MOFs inside of porous chitosan microspheres to form **MOF@CS** aerogel composites with hierarchical micro-, meso- and macro-porous network, using a supercritical CO_2 drying process. In these **MOF@CS** nanocomposites, the MOF crystals provide substantial microporous network that confine active metal sites, while macro-porous chitosan constitutes a flexible mold to hold and shape the whole material body as three-dimensional microspheres. The resulting porous catalysts were used for oxime oxidation, a challenging reaction with many industrial benefits. Owing to their large surface area, fine dispersion of MOF crystals within the polysaccharide nanofibrils, and their easy handling and recovery, **HKUST-1@CS** beads exhibit excellent activity, selectivity and reusability for the oxidation of different oximes, including the transformation of carvoxime to the industrially relevant carvone precursor.

Experimental

General remarks

$Zn(NO_3)_2.6H_2O$, $Cu(NO_3)_2.2.5H_2O$, $Fe(NO_3)_3.9H_2O$ and $Co(NO_3)_2.6H_2O$, 2-methylimidazol, trimesic acid, absolute ethanol, acetic acid (99%) and DMF were obtained from Sigma Aldrich, and used without any further purification. Chitosan, low molecular weight (viscosity 20-300 Cp) and deacetylation degree of 75-85% (CAS number 9012-76-4) was supplied by sigma Aldrich, and used as received.

Typical synthesis of MOF@CS aerogels

2 g of low molecular weight chitosan powder was dissolved in 50 mL acetic acid aqueous solution [1% (W/W)] and stirred for 24h. Next, a selected metal precursor ($Zn(NO_3)_2{\cdot}6H_2O$, $Cu(NO_3)_2{\cdot}2.5H_2O$, $Fe(NO_3)_3{\cdot}9H_2O$ and $Co(NO_3)_2{\cdot}6H_2O$) with 2:1 molar ratio with respect to NH_2 belonging to chitosan (5.8 $mmol.g^{-1}$) was added to the transparent solution. The resulting mixture was stirred for additional 2 h at room temperature until complete homogenization. Dropping this solution into a NaOH bath (4 N) using a syringe induces spontaneous chitosan gelation into porous beads. After five hours in the alkaline solution, the beads were copiously washed by distilled water until the aqueous phase approached neutral pH, and then dehydrated for 15 minutes by immersion in a series of successive ethanol-water (10-90, 30-70, 50-50, 70-30, 90-10) until 100% ethanol.[26] The beads were next placed in an alcoholic solution containing the ligand. The uptake of the ligand inside and its further condensation with the previously entrapped metal triggers the growth of the MOF crystals inside of the beads. Lastly, the resulting **MOF@CS** nanocomposites are dried under CO_2 supercritical conditions (T = 35°C, P = 73bar). Specific experimental conditions are given in Table S1. For comparison, pure chitosan beads, denoted as **CS**, were also prepared from chitosan solution without metal salt, and dried under similar supercritical conditions.

Procedure for MOF@CS aerogel catalyzed oxidation

Oxime reagent (0.5 mmol) and selected catalyst (0.010 g) were introduced into the reactor (3 mL capacity) together with appropriate volume of solvent (1 mL). The reactor was then filled

with oxygen at a pressure of 5 bar after three purges. The reaction mixture was then heated at different temperature (80°C, 100°C and 130°C) under stirring during the selected time. At the end of the reaction, the reactor was cooled and then degassed. The crude reaction product was recovered after filtration, and accurately analyzed. Dodecane was used as an external standard.

Results and Discussion

2.1. Preparation and characterization of MOF@CS aerogels

The multistep preparation of **MOF@CS** aerogel beads is illustrated in Scheme 1. As exemplified for **HKUST-1@CS**, the starting $Cu(NO_3)_2$ solution was mixed with chitosan solution to form polymer-coordinated Cu^{2+}-chitosan, due to the well-established interaction of the amino groups belonging to chitosan with the Lewis acidic metal ions through $NH_2 \rightarrow Cu$.[31] Adding this homogeneous Cu^{2+}-chitosan solution into a base bath of NaOH induces spontaneous coagulation of the whole material in form of porous microspheres, because of the insolubility of chitosan under such basic conditions. Immersing these beads in a ligand solution resulted in scavenging the latter inside of the beads where ligand-to-metal coordination takes place at the expense of $NH_2 \rightarrow Cu$, followed by the framework expansion. The as-prepared **HKUST-1@CS** alcogels are next dried under supercritical conditions using CO_2 without additional hydrothermal treatment. The use of carbon dioxide is privileged compared to water or alcohol because it reaches supercritical state at a low temperature of 31°C, compared to 373°C required for water and 513°C necessary for ethanol, making it suitable to dry soft-materials similar to those based on polysaccharides. Consequently, **HKUST-1@CS** alcogel microspheres could be converted into highly porous aerogel without noticeable damage or structural decomposition of the corresponding material. This straightforward method was successfully expanded to other metals and ligands, allowing the preparation of **ZIF-67@CS**, **ZIF-8@CS** and **Fe-BTC@CS**; all of them could be shaped as regular millimetric microspheres, dried under CO_2, and isolated as unshrinkable porous beads. The preservation of the microsphere dimension during the passage from alcogels to aerogels constitutes the first evidence of the successful drying of the porous network and the absence of severe collapsing or densification.

FTIR spectra of **MOF@CS** shows the fingerprint of both chitosan and MOF (Figure S1). All the nanocomposites show typical absorption peaks of chitosan, namely the amine band (NH_2) at 1568 cm^{-1} and the carbonyl band (C=O-NHMe) at 1650 cm^{-1}.[32] Besides, new absorption bands corresponding to the metal-organic coordination and metal-chitosan chelation could be also observed. Specifically, we have observed two absorption bands for **HKUST-1@CS** and **Fe-BTC@CS**, at 727 cm^{-1} and 630 cm^{-1}, which are respectively assigned to Cu-O and Fe-O stretching.[16,27] Both of these materials display also a new band at 1371 cm^{-1}, assignable to C=C stretching of the trimesic acid ligand.[33,34] We have also noticed a substantial decrease of the absorption intensity of -NH_2 and C=O-NHMe (1570-1640 cm^{-1}), which could be caused by the strong interaction between the metal and these N-containing groups.[31,32] **HKUST-1@CS** displays also new bands at 454-477 cm^{-1}, very characteristic of N→ Cu stretching band, which further consolidate the occurrence of intimate interplay between chitosan and MOF functionalities.[35] In the case of **ZIF-67@CS**, the bands at 500-800 cm^{-1} and at 1443 cm^{-1} are attributed to the aromatic ring out-of-plane bending and methyl bending of 2-methylimidazole, respectively.[36] In addition, the absorption band at 485 cm^{-1} could be attributed to Co-N stretching, where N comes from either the organic ligand of 2-methylimidazole or chitosan. Indeed, FTIR spectroscopy confirms the presence of both chitosan and MOF constituents inside of the dried microspheres.

In XRD, while native chitosan beads display only a broad amorphous peak at 20.4°,[27] diffraction peaks of **HKUST-1@CS**, **ZIF-67@CS**, **ZIF-8@CS** and **Fe-BTC@CS** (Figure S2) exhibit crystalline peaks that match perfectly the structure of their native HKUST-1, ZIF-67, ZIF-8 and Fe-BTC MOF, respectively.[37–39] This constitutes a salient evidence for the formation of an extended crystalline metal-organic framework inside of chitosan aerogels.

SEM and HRTEM analyses allow visualization of the expanded crystalline network grown inside of chitosan microspheres (Figure 1, Figure 2). In **HKUST-1@CS**, truncated particles with an octahedral shape and an average size of 14 µm were observed on the external surface of the aerogel beads (Figure 1a,b and Figure S3a). Besides, ultra-small sized HKUST-1 particles of ~ 3.5 nm could be also observed inside the aerogel matrix (Figure 2). The significant difference in size between the particles formed on the top surface and the ones grown can be explained by two factors: small particles can be attributed to the confinement effect occurring inside of the microspheres where the nitrogen-containing functional groups could inhibit the growth of HKUST-1. Large MOF particles could be formed by seeding the metal located on the outer-surface, near to the homogeneous solution, where much freedom and space are available for the network expansion. It should be noted that under CO_2-supercritical drying, the metal could diffuse to the outer-sphere surface for the reasons of solubility which may account for such phenomena. No external growth of MOF crystals could be however observed for **ZIF-8@CS, Fe-BTC@CS** and **ZIF-67@CS** aerogels, where the successive coordination-expansion occurs exclusively inside of the beads (Figure 1(c-h)).

Typically entangled micro-fibrils of the CO_2-dried chitosan aerogels were seen in SEM images,[40] with the presence of discrete clusters attributed to the crystalline MOFs grown inside of the polysaccharide network. Regular spherical pores were observed for **ZIF-67@CS**. This could be related to the presence of nucleating sites of ZIF-67, that act later as a porogen system because of the occurrence of phase separation within CO_2 medium (Figure 2d). Mapping the location of carbon and nitrogen versus the metal (i.e., Cu, Zn, Fe and Co) reveals the uniform distribution of these elements inside of the microspheres (Figure 2d-f, S3 and S4). Metal loading measured from ICP analysis was found to be 24% for **HKUST-1@CS**, 25% for **ZIF-67@CS**, 23% for **ZIF-8@CS** and 20% for **Fe-BTC@CS** (Table S2). The loading was in agreement with those estimated from EDX analyses and in consistency with the mineral char residue harvested at 700°C in thermogravimetric analysis (Figure S5). According to the structure formula of the corresponding MOFs (*i.e.*, HKUST-1, $C_{18}H_6Cu_3O_{12}$; ZIF-67, $C_8H_{10}N_4Co$; Fe-BTC, $C_9H_3FeO_6$), the MOFs loading in **HKUST-**

1@CS, ZIF-67@CS, ZIF-8@CS and **Fe- BTC@CS** is nearly 73%, 79%, 74% and 76% (Table S2).

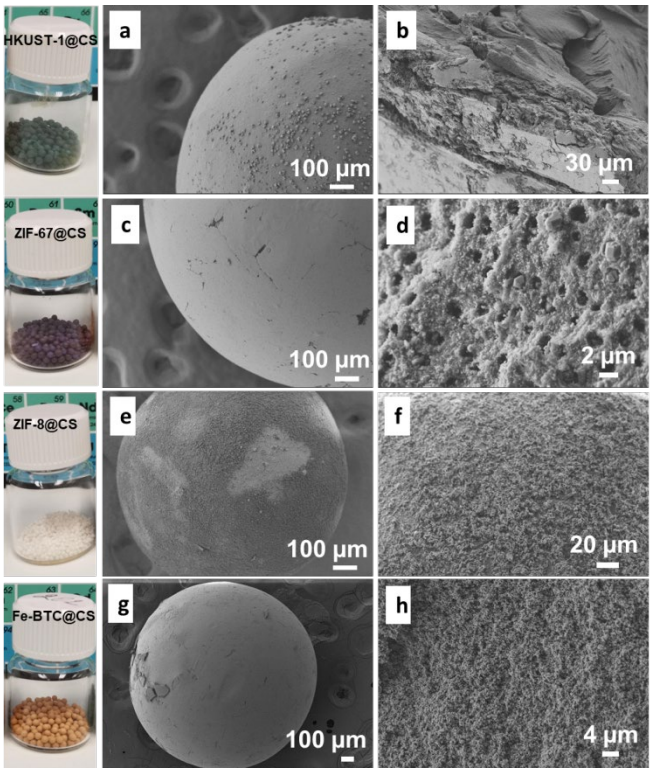

Figure 1. digital photos and the corresponding SEM images of: **HKUST-1@CS** (a,b), **ZIF-67@CS** (c,d), **ZIF-8@CS** (e,f) and **Fe-BTC@CS** (g,h).

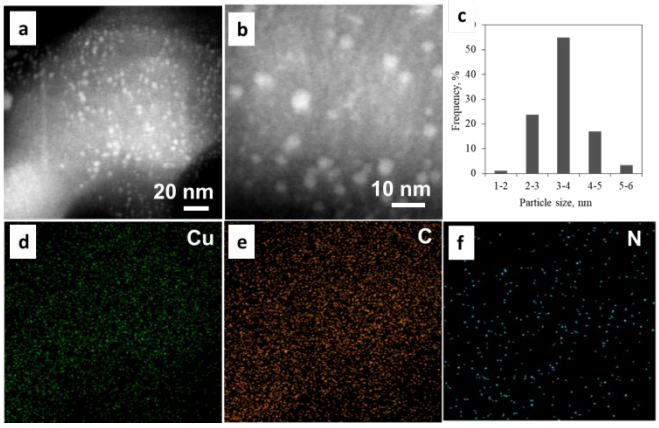

Figure 2. (a)-(b): STEM images of **HKUST-1@CS** beads; (c): particle size histogram of HKUST-1 confined inside **HKUST-1@CS** aerogel beads; (d)-(f): EDS mapping of (d) copper, (e) carbon and (f) Nitrogen.

Nitrogen sorption reveals an open porous framework for these aerogels (Figure S6). All **MOF@CS** nanocomposites exhibit an isotherm profile of large mesopores that continuously extend to the macroporous regime. This pattern is very typical of chitosan aerogels for which the entanglement of the fibrils was shown to form large mesoporous connected to the macropores. The specific surface area of **HKUST-1@CS, ZIF-67@CS**, **ZIF-8@CS**, **Fe-BTC@CS** are 531, 283, 232, 163 $m^2.g^{-1}$, respectively. Their increased surface area compared to native chitosan microspheres (120 $m^2.g^{-1}$) indicates that the extended network of MOF does not reduce the accessible surface area in the dried aerogels, in spite of the highest amount of the loaded objects. In contrast, it seems that the presence of metal-coordination framework in the wetted hydrogels sustain the preparation of porous aerogels probably through swelling hydrogels,[27] or by altering hydrogen bonding between adjacent biopolymer fibrillar chains that could be drawn together during solvent exchange or removal necessary for polysaccharide drying.[26] Similar "swelling induced expansion" was previously observed during the growth of titanium dioxide clusters inside of chitosan alcogel microspheres.[41] The highest surface area of **HKUST-1@CS** can be attributed to the significant contribution of HKUST-1 microporosity. This indicates that despite their confinement inside of the microspheres, the intrinsic microporosity of the MOF remains accessible for nitrogen uptake. Such hierarchical porosity presents a tremendous interest in heterogeneous catalysis, with the micropores being associated to the confinement effect while the macropores allow faster molecular traffic thereby reducing the thermodynamic barrier related to the mass transfer.

Insight on the chemical composition was gained by comparative XPS analysis of **HKUST-1**, **Cu@CS** and **HKUST-1@CS** (Figure S7). N(1s) spectra was deconvoluted into two peaks with binding energies at (397.6±0.2 eV) and (399.04±0.2 eV), which can be attributed to free NH_2 groups and the coordinated NH_2--->Cu, respectively. This further corroborates the intimate interaction of Cu species with nitrogen.[42] A close look on the XPS spectra of Cu 2p3/2 in the three materials (**HKUST-1**, **Cu@CS** and **HKUST-1@CS**) reveals as shown in Figure S7, an intensive broad lines at 934.7 eV for **Cu@CS** and at 934.5 eV for **HKUST-1@CS** accompanied by satellites centered around at 939–945eV correspond to the Cu^{2+} state.[43,44] The similarities between the XPS profile of HKUST-1 and **HKUST@CS** indicate that most of copper entrapped in chitosan microspheres is coordinated to HKUST-1, which exclude the predominance of nanosized copper or molecular copper that could be ligated to chitosan.[45]

Thermal stability of these nanocomposites was further assessed using TGA (Figure S5). While native chitosan microspheres loss their total weight at nearly 580°C, the resulting hybrid aerogels display a chare residue varying from 16 wt% to 23 wt% up to 800°C. This harvested solid can be attributed to the conversion of the MOF into the corresponding ceramic phase (CuO for instance in the case of **HKUST-1@CS).** Subjecting these beads to thermal annealing treatment under nitrogen atmosphere reveals their stability. While a color change has been observed (Figure 3a,b), the shape of the microsphere and the crystalline structure of the corresponding MOF are preserved as illustrated through SEM and XRD analysis (Figure 3c-e, Figure S8-a). TEM images reveals the presence of small sized nanoparticles with 3.9 nm in diameter while element mapping confirms homogenous distribution of carbon, nitrogen and copper inside (Figure 3f). Despite the harsh thermal treatment, the resulting beads display significant porosity, with specific surface areas above 120 $m^2.g^{-1}$, meaning that the presence of MOF significantly sustain the stability of the polysaccharide skeletal (Table S2, Figure S8-b). The following **MOF@CS** nanocomposites can be indeed used for heterogeneous catalysis requiring up to 200°C thermal activation. Noteworthy is the attractiveness of this **MOF@CS** carbonization

route expected to open another channel of possibilities by providing novel MOF-derived nanostructures.[46,47]

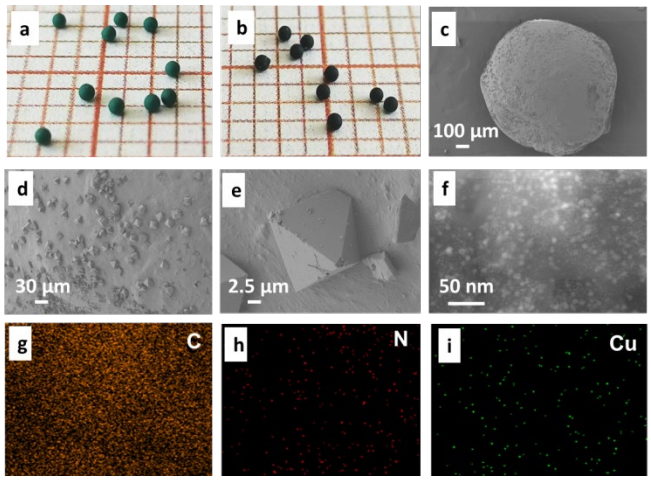

Figure 3. Digital photos of **HKUST-1@CS** before (a) and after (b) pyrolysis at 200°C under N_2 flow; (c)-(e) SEM images of **HKUST@CS** beads; (f) STEM image and EDS mapping of carbon (g), nitrogen (h) and copper (i).

2.2. Catalytic studies

Oxidation of oximes into the corresponding carbonyl compounds is an industrially important transformation. For instance, cyclohexanone derivatives are annually produced in large scale from cyclohexanone oximes and serve as precursors to nylon.[48] Oxime oxidation has been conducted both under homogeneous and heterogeneous conditions.[49,50] Au/CeO_2 and Pt/CeO_2 have been proven to be highly active and selective for oxime oxidation to corresponding carbonyl compounds.[51] Non-noble metal based catalysts, like mixed (Fe^{2+} and Cu^{2+}) double metal hexacyanocobaltates, have also been tested for such purpose.[52] However, the development of low-cost and durable catalysts is still crucial to further promote this key industrial transformation.

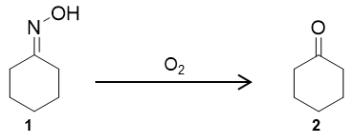

Scheme 2. Oxidative conversion of cyclohexanone oxime **1** into cyclohexanone **2**.

We have indeed embarked to assess the catalytic activity of these MOF-shaped aerogels. First, no catalytic activity could be detected using native **CS** chitosan aerogels. In contrast, all **MOF@CS** nanocomposites displayed noticeable activity and are selective toward cyclohexanone **2** (Figure 4a). When operating at 80°C, **ZIF-8@CS** exhibited very limited catalytic activity, giving only 5% yield of **2**. **Fe-BTC@CS** and **ZIF-67@CS** demonstrated higher oxidation activity, affording 17% and 24% yields, respectively. Interestingly, **HKUST-1@CS** affords 90% yield of **2**. Temperature seems to boost the catalytic activity of these materials, as exemplified by 27 % and 41% yields obtained at 100°C with **Fe-BTC@CS** and **ZIF-67@CS**, respectively, while in the case of **HKUST-1@CS**, the reaction reaches 100 % in a short reaction time of 3h. Further increase of the reaction temperature to 130 °C resulted in higher conversions with **ZIF-8@CS, Fe-BTC@CS** and **ZIF-67@CS** (nearly 90%) but leads unfortunately to severe structural damage of the aerogel beads. The use of only half amount of **HKUST-1@CS** (4 wt% instead of 8 wt%), at 100°C for 4h, affords **2** in 66% yield, which suggest the superior activity of **HKUST-1@CS** over its partners. Figure S9 displays the time-yield plots for the oxidation of **1** to **2** in the presence of **HKUST-1@CS** at different temperatures. The activation energies (Ea) obtained from the slope of the best fitting of the experiment points to a straight line and applying the Arrhenius equation [lnk = -Ea/RT + lnA] with **HKUST-1@CS, ZIF-67@CS** and **Fe(MOF)@CS** were 61.5, 63.2 and 64.8 kJ/mol, respectively (Figure S10).

Considering the pivotal role of the solvent in this reaction type, we have also investigated the behavior of these microspheres in different liquid phase medium (Figure 4b). The highest activity was reached using ethanol: water (1:1, v:v), given rise to 67% conversion of **1** at 130 °C after 0.5 h. In ethanol, isopropanol and toluene, **HKUST-1@CS** showed inferior activity, affording 50%, 38% and 21% conversion, respectively. The use of ethanol-water mixture promotes indeed the catalytic performance of **HKUST-1@CS** for oxime oxidation. This result can be associated to the hydrolysis pathway that could facilitate the formation of the target cyclohexanone.[51] Additional comparative catalytic tests were performed to highlights the inherent advantages of **HKUST-1@CS** aerogels (Figure 4c). First, **HKUST-1@CS** xerogel, where the alcogel beads were dried under air, was devoid of any catalytic activity (3% conversion). As the drying was performed under air, the resulting **HKUST-1@CS** xerogels shrinks severely because of the meniscus formed during liquid removal from the pores. This interfacial tension exerted on the polysaccharide fibrils leads to a complete collapse of the initial porosity created in the starting hydrogels. Consequently, the entrapped MOFs are buried inside and are not accessible to the reactants. We have further prepared **Cu@CS** aerogels, where copper particles were grown on chitosan without the use of the BTC ligand. While a noticeable activity could be observed this time, allowing 69% yields to be reached, it remains less reactive compared to **HKUST-1@CS** aerogels. This indicates that the oxidation state of Cu bearing MOF is the most active and suitable form for oxime oxidation. Native **HKUST-1** alone displays 81% yield, being less active compared to **HKUST-1@CS**. The superior activity of the shaped MOF aerogels could be tentatively associated to their high surface area and hierarchical porosity and fine dispersion of HKUST inside (Figure S3, S6). These comparative results indicate the importance of the accessibility to the active copper sites reached herein through CO_2-supercritical drying. Besides, the recovery of **HKUST-1** was quite tedious, necessitating the use of filters while in the case of **HKUST-1@CS**, the millimitric microspheres could be straightforwardly removed by a spatula.

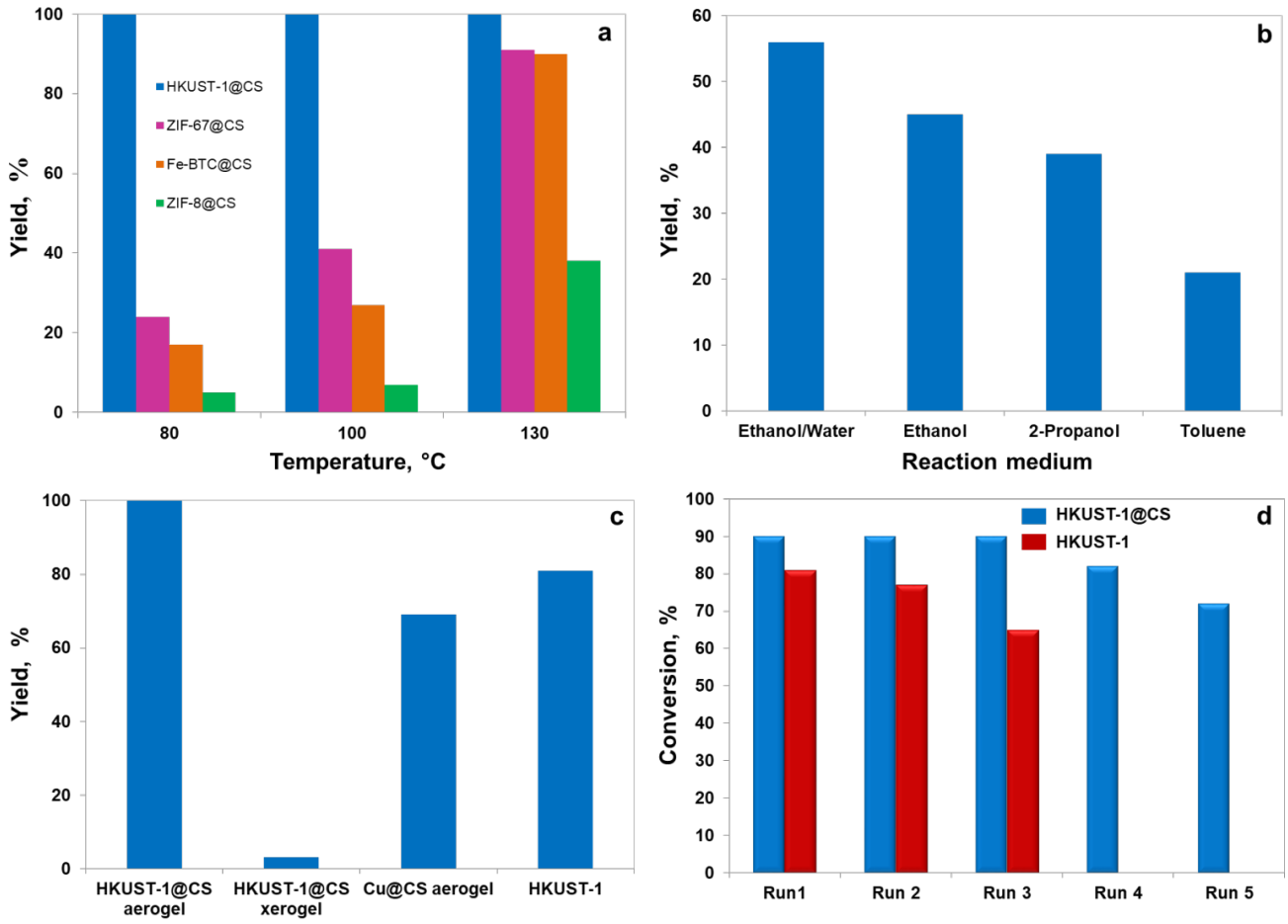

Figure 4. (a) Catalytic performance of different **MOF@CS** aerogels in the selective oxidation of **1** to **2**, reaction condition: 0.8 mmol reactant, 1 mL ethanol/water (1/1, v/v), catalyst/reactant solution ratio 8 wt.%, 5 bar O_2, 6 h. For **HKUST-1@CS**, yield of **2** reached 100% after 4 h and 3 h at 100 °C and 130 °C, respectively; (b) catalytic performance of **HKUST-1@CS** in different solvents; (c) comparative catalysis using different copper-supported on chitosan; (d) Recycling of **HKUST-1@CS** and HKUST-1 in the selective oxidation of **1** to **2**, reaction condition: 0.8 mmol reactant, 1 mL ethanol/water (1/1, v/v), catalyst/reactant solution ratio 8 wt.%, 80 °C, 5 bar O_2, 6 h.

Next, hot filtration test was performed to confirm whether the catalyst is true heterogeneous or works through a release and catch catalytic process. Removal of **HKUST@CS** microspheres from the medium after half an hour of the reaction progress indicated the stagnation of the conversion at the 68% conversion with no more consumption of the starting reactant. Interestingly, even under challenging temperature conditions of 130°C, no catalysis could be observed after **HKUST@CS** removal, which suggest the tight incorporation and ligation of copper inside of the aerogels (Figure S12). These assumptions have been next consolidated by ICP analyses where the amount of copper released to the liquid medium was only 0.009%, witnessing on the absence of significant metal leaching, despite the challenges faced with copper species that are more labile and prone lo leaching.

As stated above, the recovery of the catalyst was straightforward. The recovered microspheres were placed again in a new catalytic medium and were used several times with new reactants. In concrete terms, **HKUST-1@CS** aerogel was able to retain full conversion during the first three runs (Figure 4d). A marginal decrease of their catalyst activity was next noticed after five cycles but **HKUST-1@CS** remains active, allowing 72% conversion of the reactant. In contrast, **HKUST-1** deactivation started early, allowing only 65% of conversion of **1** after their third use. Taking together, one may easily spotlight the advantages imparted by shaping MOF catalysts for their recovery and reuse although further optimization and studies are still needed to maintain the catalyst stability. The catalyst was recovered, washed and dried before further characterization by XRD and XPS (Figure S13). The XRD diffractogram confirmed the retention of the framework crystallinity after 5 cycles while XPS studies of Cu2p suggested the loss of N--->Cu coordination that was initially observed for native catalyst. This could be attributed to the inherent properties of chitosan that is prone to deactivation probably under oxidizing conditions as it has been previously observed.[31]

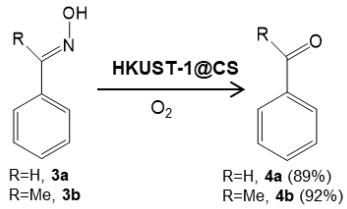

Scheme 3. Oxidation of oximes using **HKUST-1@CS**. **3a**: benzaldehyde oxime, **3b**: acetophenone oxime, **4a**: benzaldehyde, **4b**: acetopheneone. Reaction conditions: 0.8 mmol reactant, 1 mL ethanol/water (1/1, v/v), catalyst/reactant solution ratio 8 wt.%, 130 °C, 5 bar O_2, 6 h.

We next attempted the oxidation of acetophenone-oxime and benzaldehyde-oxime into the corresponding acetophenone and benzaldehyde (Scheme 3). After exposure to **HKUST-1@CS** during 6h at 130°C, under 5 bar pressure of oxygen, 89% yield of acetophenone and 92% yield of benzaldehyde could be obtained, respectively. This indicates that **HKUST-1@CS** aerogel is also efficient for the selective transformation of keto- and ald-oximes.

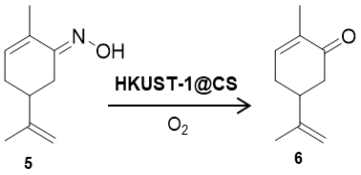

Scheme 4. Oxidative conversion of **5** (carvone oxime) to **6** (carvone)

We lastly turned our attention to the preparation of carvone, which is ubiquitous in many essential oils (65% of spearmint oil is 1-carvone and *d*-carvone is the major constituent of caraway and dill seed oils), and consequently, very important as a building-block.[53,54] **HKUST@CS** displays excellent catalytic carvoxime oxidation ability (figure S14). At T=80 °C, the conversion of **5** reaches 82 % yield after 20h. Increasing the reaction temperature to 100°C allows an almost quantitative yield. Further increase of the temperature to 130 °C speeds the reaction that reaches quantitative yield in only 8h. Besides, no epoxide or other oxygen containing side products could be detected, with carvone selectivity being of 100%. The activation energy obtained from the slope of the best fitting of the experiment points to a straight line and applying the Arrhenius equation [lnk = -Ea/RT + lnA] with **HKUST-1@CS** was 72.8 kJ/mol.

Conclusions

In summary, we herein investigate the expansion and growth of the so-called metal-organic frameworks inside of chitosan microspheres. The templating effect of chitosan hydrogels was found to be suitable to grow a library of **MOF@CS** composites including **HKUST-1@CS**, **ZIF-8@CS**, **ZIF-67@CS**, and **Fe-BTC@CS**. CO_2-supercritical drying of the resulting soft alcogels resulted in an open porous framework of entangled polysaccharide micro-fibrils holding well-dispersed MOF clusters. While an impressive amount of MOF could be loaded within the microspheres, an increase in the specific surface area was observed, suggesting a positive effect of the MOF for sustaining the open porous framework during the hydrogel drying step, through swelling and disrupting interchain hydrogen-bonding. The resulting porous aerogels, especially **HKUST-1@CS**, showed excellent catalytic performance (activity, selectivity and reusability) in the selective oxidation of different oximes to carbonyl-containing fine chemical including the highly desired carvone synthesis. The high catalytic performance of **HKUST-1@CS** relies on its high surface area, fine dispersion of **HKUST-1** crystals and the specific chemical and electrical environment of Cu species. The process is heterogeneous and the catalysts can be reused several times without significant deactivation. The process described here fulfills most of the requirements of green chemistry and can replace the currently used Brönsted acids that are notoriously unsatisfactory from the environment point of view due to corrosion and the generation of aqueous waste.

Acknowledgements

NH thanks UEMF and UPV for an Erasmus+ 2019-1-ES01-KA107-062073 Scholarship. AEK thanks UEMF for funding. Partenariat Hubert Curien – Toubkal (project No.18/40) is acknowledged for supporting and funding partially this work. Chevreul Institute (FR 2638), Ministère de l'Enseignement Supérieur et de la Recherche, Région Hauts-de-France and FEDER are acknowledged for funding. The authors also thank technical support from the Lille University: Martine Trentesaux and Pardis Simon for XPS analysis, Olivier Gardoll for TGA analysis, Laurence Burylo for XRD experiment.

References

1 H. C. Zhou, J. R. Long, O.M. *Chem. Rev.*, 2012, **112**, 673–674.
2 V. Pascanu, G. González Miera, A. K. Inge and B. Martín-Matute, *J. Am. Chem. Soc.*, 2019, **141**, 7223–7234.
3 A. Dhakshinamoorthy, Z. Li and H. Garcia, *Chem. Soc. Rev.*, 2018, **47**, 8134–8172.
4 A. Dhakshinamoorthy and H. Garcia, *Chem. Soc. Rev.*, 2012, **41**, 5262–5284.
5 S. M. J. Rogge, A. Bavykina, J. Hajek, H. Garcia, A. I. Olivos-Suarez, A. Sepúlveda-Escribano, A. Vimont, G. Clet, P. Bazin, F. Kapteijn, M. Daturi, E. V. Ramos-Fernandez, F. X. L. i Xamena, V. V. Speybroeck and J. Gascon, *Chem. Soc. Rev.*, 2017, **46**, 3134–3184.
6 H. Deng, C. J. Doonan, H. Furukawa, R. B. Ferreira, J. Towne, C. B. Knobler, B. Wang and O. M. Yaghi, *Science*, 2010, **327**, 846–850.
7 H. Furukawa, N. Ko, Y. B. Go, N. Aratani, S. B. Choi, E. Choi, A. Ö. Yazaydin, R. Q. Snurr, M. O'Keeffe, J. Kim and O. M. Yaghi, *Science*, 2010, **329**, 424–428.
8 V. R. Remya and M. Kurian, *Int. Nano Lett.*, 2019, **9**, 17–29.
9 T. Kitao, Y. Zhang, S. Kitagawa, B. Wang and T. Uemura, *Chem. Soc. Rev.*, 2017, **46**, 3108–3133.
10 S. El Hankari, M. Bousmina and A. El Kadib, *Prog. Mater. Sci.*, 2019, **106**, 100579.
11 P. Falcaro, R. Ricco, A. Yazdi, I. Imaz, S. Furukawa, D. Maspoch, R. Ameloot, J. D. Evans and C. J. Doonan, *Coord. Chem. Rev.*, 2016, **307**, 237–254.
12 Q.-L. Zhu and Q. Xu, *Chem. Soc. Rev.*, 2014, **43**, 5468–5512.

13 D. Bradshaw, A. Garai and J. Huo, *Chem. Soc. Rev.*, 2012, **41**, 2344–2381.
14 D. Bradshaw, S. El-Hankari and L. Lupica-Spagnolo, *Chem. Soc. Rev.*, 2014, **43**, 5431–5443.
15 M. Ding, X. Cai and H.-L. Jiang, *Chem. Sci. J.*, 2019, **10**, 10209–10230.
16 N. Hammi, S. El Hankari, N. Katir, N. Marcotte, K. Draoui, S. Royer and A. El Kadib, *Micropor. Mesopor. Mat.*, 2020, **306**, 110429.
17 S. S. Nadar, L. Vaidya, S. Maurya and V. K. Rathod, *Coord. Chem. Rev.*, 2019, **396**, 1–21.
18 M. Kalaj, K. C. Bentz, S. Ayala, J. M. Palomba, K. S. Barcus, Y. Katayama and S. M. Cohen, *Chem. Rev.*, 2020, **120**, 8267–8302.
19 A. E. Kadib, M. Bousmina and D. Brunel, J. Nanosci. Nanotechnol., 2014, **14**, 308–331.
20 A. El Kadib and M. Bousmina, *Chem. Eur. J.*, 2012, **18**, 8264–8277.
21 N. Hammi, N. Wrońska, N. Katir, K. Lisowska, N. Marcotte, T. Cacciaguerra, M. Bryszewska and A. El Kadib, *ACS Appl. Bio Mater.*, 2019, **2**, 61–69.
22 A. Primo, F. Quignard, Chem. Commun., 2010,46, 5593-5595
23 S. Frindy, A. Primo, A. el kacem Qaiss, R. Bouhfid, M. Lahcini, H. Garcia, M. Bousmina and A. El Kadib, *Carbohydr. Polym.,* 2016, **146**, 353–361.
24 S. Frindy, A. Primo, H. Ennajih, A. el kacem Qaiss, R. Bouhfid, M. Lahcini, E. M. Essassi, H. Garcia and A. El Kadib, Carbohydr. Polym., 2017, **167**, 297–305.
25 A. El Kadib, *Chem. Rec.*, 2020, **20**, 753–772.
26 R. Valentin, K. Molvinger, F. Quignard and D. Brunel, New J Chem., 2003, **27**, 1690–1692.
27 R. Zhao, T. Ma, S. Zhao, H. Rong, Y. Tian and G. Zhu, *Chem. Eng. Sci.*, 2020, **382**, 122893.
28 N. Baccile, J. Reboul, B. Blanc, B. Coq, P. Lacroix-Desmazes, M. In and C. Gérardin, *Angew. Chem. Int. Ed.,* 2008, **120**, 8561–8565.
29 Z. Inonu, S. Keskin and C. Erkey, *ACS Appl. Nano Mater.*, 2018, **1**, 5959–5980.
30 L. Zhu, L. Zong, X. Wu, M. Li, H. Wang, J. You and C. Li, *ACS Nano*, 2018, **12**, 4462–4468.
31 S. Frindy, A. El Kadib, M. Lahcini, A. Primo and H. García, *ChemCatChem*, 2015, **7**, 3307–3315.
32 A. E. Kadib, K. Molvinger, M. Bousmina and D. Brunel, *J. Catal.*, 2010, **273**, 147–155.
33 S. Lin, Z. Song, G. Che, A. Ren, P. Li, C. Liu and J. Zhang, *Micropor. Mesopor. Mat.*, 2014, **193**, 27–34.
34 F. Ahmad Sofi, M. Ahmad Bhat and K. Majid, New. *J. Chem.,* 2019, **43**, 3119–3127.
35 O. Jennah, R. Beniazza, C. Lozach, D. Jardel, F. Molton, C. Duboc, T. Buffeteau, A. El Kadib, D. Lastécouères, M. Lahcini and J.-M. Vincent, *Adv. Synth. Catal.*, 2018, **360**, 4615–4624.
36 S. Fazlifard, T. Mohammadi and O. Bakhtiari, *Chem. Eng. Technol.*, 2017, **40**, 648–655.
37 X. Zhang, J. Chen, X. Pei, J. Wang, Q. Wan, S. Jiang, C. Huang and X. Pei, *ACS Appl. Mater. Interfaces*, 2017, **9**, 25171–25183.
38 J. Cao, C. Lei, J. Yang, X. Cheng, Z. Li, B. Yang, X. Zhang, L. Lei, Y. Hou and Kostya (Ken) Ostrikov, *J. Mater. Chem. A.*, 2018, **6**, 18877–18883.
39 M. R. Azhar, H. R. Abid, H. Sun, V. Periasamy, M. O. Tadé and S. Wang, *J. Colloid Interface Sci.*, 2016, **478**, 344–352.
40 S. Takeshita and S. Yoda, *Chem. Mater.*, 2015, **27**, 7569–7572.
41 A. E. Kadib, K. Molvinger, C. Guimon, F. Quignard and D. Brunel, *Chem. Mater.*, 2008, **20**, 2198–2204.
42 B. Vafakish and L. D. Wilson, *Molecules*, 2020, **25**, 1052.
43 A. Domán, B. Nagy, L. P. Nichele, D. Srankó, J. Madarász and K. László, *Appl. Surf. Sci.*, 2018, **434**, 1300–1310.
44 S. Basumallick, P. Rajasekaran, L. Tetard and S. Santra, *J Nanopart Res.*, 2014, **16**, 2675.
45 G. Huang, J. Chen, X. Tang, D. Xiong, Z. Liu, J. Wu, W.-Y. Sun and B. Lin, *ACS Appl. Mater. Interfaces.*, 2019, **11**, 10389–10398.
46 M. Bagheri, A. Melillo, B. Ferrer, M. Y. Masoomi and H. Garcia, *Chem. Eur. J.*, 2021, **27**, 14273–14281.
47 M. Bagheri, A. Melillo, B. Ferrer, M. Yaser Masoomi and H. Garcia, Chem. Commun., DOI:10.1039/D1CC05182B.
48 R. Mokaya and M. Poliakoff, *Nature*, 2005, **437**, 1243–1244.
49 B. A. Mendelsohn, S. Lee, S. Kim, F. Teyssier, V. S. Aulakh and M. A. Ciufolini, *Org. Lett.*, 2009, **11**, 1539–1542.
50 A. Corsaro, M. A. Chiacchio and V. Pistara, *Curr. Org. Chem.,* 2009, **13**, 482–501.
51 A. Grirrane, A. Corma and H. Garcia, *J. Catal.*, 2009, **268**, 350–355.
52 A García-Ortiz, A Grirrane, E Reguera, H García, *J. Catal.*, 2014, **311**, 386–392
53 C. Bordenca, R. K. Allison and P. H. Dirstine, *Ind. Eng. Chem.*, 1951, **43**, 1196–1198.
54 C. C. C. R. de Carvalho and M. M. R. da Fonseca, *Food Chem.*, 2006, **95**, 413–422.